J. Phys. B: At. Mol. Opt Phys. 28 (1995) 4907–4925. Printed in the UK

Hyperspherical close-coupling calculation of positronium formation and excitation cross sections in positron–hydrogen scattering at energies below the H($n = 4$) threshold

Yan Zhou and C D Lin

Department of Physics, Kansas State University, Manhattan, KS 66506, USA

Received 8 June 1995, in final form 21 August 1995

Abstract. A hyperspherical close-coupling method is used to calculate the elastic, positronium formation and excitation cross sections for positron collisions with atomic hydrogen at energies below the H($n = 4$) threshold for $L = 0$ and 1 partial waves. A new two-dimensional coordinate transformation is used such that the Schrodinger equation at large hyper-radii can be solved accurately. The coupled hyper-radial equations are integrated to a large hyper-radius at which the solution is matched to the dipole states in the outer region. From the extracted K-matrix, the elastic, positronium formation and atomic hydrogen excitation cross sections are computed. Resonance positions, total widths, and partial cross sections are also examined and compared with those from other calculations.

1. Introduction

The scattering of positrons with atomic hydrogen has long been an interesting theoretical subject. It is one of the simplest Coulomb three-body systems, but the existence of rearrangement channels makes it a major challenge for theoretical description. Over the years, different methods have been suggested. For a more comprehensive review of methods used thus far and available experimental results, the readers are referred to recent papers (Humberston and Armour 1987, Zhou and Lin 1994, Mitroy and Ratnavelu 1995) and references therein. Briefly, the most commonly used approach is based on the close-coupling method using orbitals of atomic hydrogen and positronium as basis functions. In some calculations, pseudostates are also included to account for the short- and long-range correlations. But the inclusion of two-centre basis functions may cause pseudoresonances (Basu *et al* 1989, Higgins and Burke 1991, Sarkar *et al* 1993, Zhou and Lin 1995b), and the result depends sensitively on the number of basis functions employed as documented by Kernoghan *et al* (1994). Aside from the close-coupling approach, a variational method has been used and accurate results have been obtained. But the method is limited to the elastic scattering and the Ore gap region (the energy gap between Ps($n = 1$) and H($n = 2$) levels) only.

An alternative approach is the hyperspherical method. The method was first formulated by Smith (1960) for treating quantum atom–diatom reactive scatterings and is now widely used by quantum chemists (see Launay 1993). In atomic physics, the hyperspherical approach was first used within the adiabatic approximation and in the classification of doubly excited states of atoms (Macek 1968, Lin 1984, 1986). More recently, the development of the hyperspherical close-coupling approach (HSCC) makes it possible to obtain accurate results for resonance energies, widths and photoionization cross sections for atomic systems

0953-4075/95/224907+19$19.50

(Tang *et al* 1992, Zhou *et al* 1993, Tang and Shimamura 1995). A recent review of the hyperspherical approach up to the middle of 1994 is given in Lin (1995).

The HSCC method has also been extended to study general Coulomb three-body systems, and, in particular, the collision between positrons and atomic hydrogen. Careful calculations using the hyperspherical approach have been limited to the Ore gap region only so far, as reported by Igarashi and Toshima (1994), and by Zhou and Lin (1994). An earlier calculation by Archer *et al* (1990) covers a larger energy region, but it was limited to $J = 0$ states only and the numerical accuracy achieved in that calculation is also more limited.

In this paper, we describe the improvement in the numerical procedure used beyond what was described in our earlier paper (Zhou and Lin 1994). The modification is needed in order to be able to calculate excitation and positronium formation cross sections to higher excited states for positron–hydrogen scattering in the higher energy region, as well as the resonances in this system. To achieve this goal, we need to calculate accurate hyperspherical potential curves up to a large hyper-radius. Furthermore, since the excited states of atomic hydrogen (and the positronium) are degenerate for states of the same principal quantum number, the asymptotic wavefunctions in the dissociation limits are dipole states (Seaton 1961, Gailitis and Damburg 1963), and proper modification of the wavefunctions in the outer region in the HSCC method has to be made. A summary of the HSCC method and these modifications are discussed in section 2. The results are presented and discussed in section 3, with a summary and future improvements and applications addressed in section 4. Atomic units are used unless explicitly noted otherwise.

2. The hyperspherical close-coupling approach

2.1. Brief review of the hyperspherical close coupling approach

The three equivalent Jacobi coordinate systems for describing the three particles are defined as in figure 1. Following the definitions in Zhou and Lin (1994), the reduced wavefunctions Ψ are shown to satisfy

$$\left(-\frac{\partial^2}{\partial R^2} + H_{ad} - 2\mu E\right)\Psi(R, \phi, \hat{\Omega}) = 0 \tag{1}$$

where $\hat{\Omega}$ denotes collectively the four orientation angles of vectors ρ_1 and ρ_2, R is the hyper-radius and ϕ is the hyperangle. This equation can be expressed in any one of the three coordinate sets of figure 1. The adiabatic Hamiltonian is

$$H_{ad}(R; \phi, \hat{\Omega}) = \frac{\Lambda^2 + 2\mu R C(\phi, \theta)}{R^2} \tag{2}$$

with

$$\Lambda^2 = \left(-\frac{\partial^2}{\partial \phi^2} + \frac{l_1^2}{\cos^2\phi} + \frac{l_2^2}{\sin^2\phi}\right) - \frac{1}{4} \tag{3}$$

where l_1 and l_2 are the usual orbital angular momentum operators, and

$$C(\phi, \theta) = \sqrt{\frac{\mu_1^\alpha}{\mu}}\frac{Z_1 Z_2}{\cos\phi^\alpha} + \sqrt{\frac{\mu_1^\beta}{\mu}}\frac{Z_2 Z_3}{\cos\phi^\beta} + \sqrt{\frac{\mu_1^\gamma}{\mu}}\frac{Z_3 Z_1}{\cos\phi^\gamma} \tag{4}$$

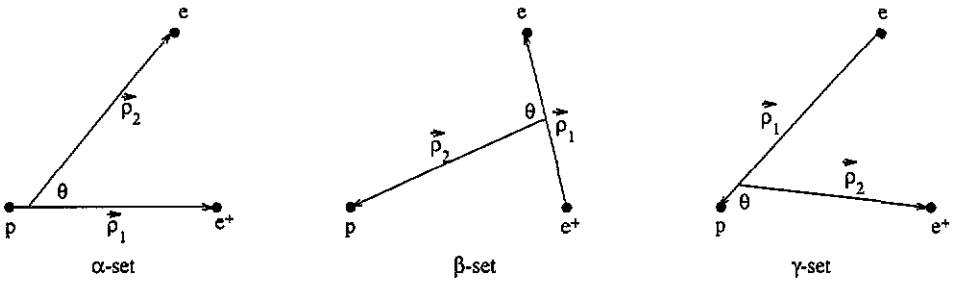

Figure 1. Definition of the three sets of Jacobi coordinates for the e^++H collision system.

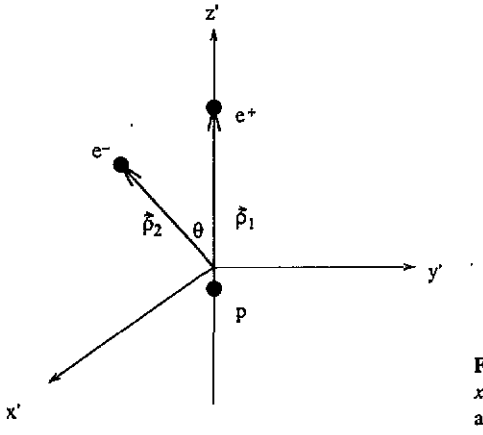

Figure 2. Body-frame axes. The three particles lie on the x'–z' plane with the z' axis along the proton–positron line and the electron is above the x'–y' plane.

is the effective charge of the three particles. In equation (4), Z_i is the charge of particle i. The angles ϕ, θ are the two internal angles expressible in any set of Jacobi coordinates, where $\cos\phi^\tau = \sqrt{\mu_1^\tau/\mu}\cdot\rho_1^\tau/R$ with $\tau = \alpha$, β or γ (for definitions of ρ_1^τ, see figure 1). The reduced mass μ_1^τ is the reduced mass of the first pair of particles in the τ-set Jacobi coordinates and μ is an overall mass scaling factor, which is taken to be unity in this paper.

We seek to solve (1) using the HSCC method. First the hyper-radius is separated into two regions at $R = R_0$. In the inside region $R \leqslant R_0$ where all three particles interact with each other, the wavefunctions are to be expressed in terms of hyperspherical coordinates. In the outer region, the three-body system breaks into a single particle and a pair of particles in some bound states. In this outer region, the wavefunctions are appropriately expressed in terms of Jacobi coordinates for each arrangement. In the HSCC method, the inner region of the hyper-radius is further divided into many small sectors. Using the so-called diabatic-by-sector method (Tang *et al* 1992), the wavefunction within each sector is expanded as

$$\Psi(R,\phi,\hat{\Omega}) = \sum_\nu \sum_l F_{\nu l}(R)\Phi_{\nu l}(R_a;\theta,\phi)\tilde{D}^J_{lM_J}(\omega_1,\omega_2,\omega_3) \tag{5}$$

where the wavefunctions are expressed in the body-frame, with the body-frame axes defined as in figure 2. In equation (5), the normalized D-function has good-parity (Bhatia and Temkin 1964), ν is the channel index, R_a is chosen at the midpoint of the sector, J is the total angular momentum, l is the absolute value of the projection of J along the body frame's z' axis and running from 0 to J for $(-1)^J P = 1$ states and from 1 to J for $(-1)^J P = -1$ states, with P being the parity.

The numerical solution of (1) is done in two steps. First, the channel functions $\Phi_{\mu I}(R_a;\theta,\phi)$ are solved in the α-set Jacobi coordinates at a set of points R_a satisfying the equation

$$\left[\frac{T_0+\langle\tilde{D}^J_{IM_J}|T_1|\tilde{D}^J_{IM_J}\rangle}{R_a^2}+\frac{2\mu C}{R_a}\right]\Phi_{\mu I}(R_a;\theta,\phi)=2\mu U_{\mu I}(R_a)\Phi_{\mu I}(R_a;\theta,\phi) \tag{6}$$

with $0\leqslant\theta\leqslant\pi$ and $0\leqslant\phi\leqslant\pi/2$. The explicit form of the operators T_0 and T_1 is given in Zhou and Lin (1994). Basically, equation (6) is a two-dimensional partial differential equation in angles (θ,ϕ). The eigenvalues in equation (6) are solved using the higher order finite element method—the details are further discussed in section 2.3 below.

Using the diabatic-by-sector method as in (5), the hyper-radial functions satisfy a set of one-dimensional coupled differential equations

$$\left(-\frac{\partial^2}{\partial R^2}-\frac{1}{4R^2}-2\mu E\right)F_{\mu I}(R)+\sum_{\nu I'}V_{\mu I,\nu I'}(R)F_{\nu I'}(R)=0 \quad . \tag{7}$$

where the coupling matrix elements V are defined explicitly in Zhou and Lin (1994) and in Lin (1995).

In the practical implementation of the HSCC method, the set of hyper-radial equations (7) is integrated within each sector. Starting with the innermost sector, the integration is continued until it reaches the boundary of the next sector. At this boundary, the total wavefunctions are expanded in terms of basis functions of the next sector from which integration within the next sector can be carried out. This procedure is continued from small hyper-radius to R_0 where the wavefunction is matched to an outside solution expressed in terms of independent electronic coordinates ρ_1,ρ_2. The details of such a procedure are given in Zhou and Lin (1994) and Lin (1995). From the matching one can extract the K-matrix and the partial scattering cross sections are obtained from

$$\sigma_{ij}^{(J)}=\frac{4\pi(2J+1)}{k^2}\left|\frac{K}{1-\mathrm{i}K}\right|_{ij}^2 \tag{8}$$

where k is the momentum of the incident particle.

In comparison with our previous work, we have implemented two new numerical procedures in order to be able to carry out the calculations reported here. They are discussed in detail in the next two subsections.

2.2. The dipole states in the outer region

The total wavefunction in the region beyond R_0 in general can be expressed as a linear combination of products of target bound states multiplied by regular and irregular Bessel functions, see equation (25) of Zhou and Lin (1994). For energies above the $n=2$ excitation threshold, the hydrogenic target eigenstates are degenerate for states with identical principal quantum number n and in the dissociation limits these states are coupled by the dipole operator (Seaton 1961, Gailitis and Damburg 1963). It is advantageous to account for this dipole interaction in the asymptotic region analytically so that the matching can be carried out at a smaller R_0. In the dipole representation (Seaton 1961, Gailitis and Damburg 1963), the channels in the outside region are labelled by quantum numbers of the dipole states which take the general form $\sum_{l\geqslant l}c_l\varphi_{nl}$, i.e. in terms of a linear combination of hydrogenic states.

The use of these new basis functions in the asymptotic region results in the modification in the definition of the matching matrix elements. For example, the $\varphi_\lambda f_\lambda S_{l_1^\tau l_2^\tau JM_JP}$ term in (32) of Zhou and Lin (1994) should be replaced by $\sum_\nu t_{\lambda\nu}\varphi_\nu f_\lambda S_{l_1^\tau l_2^\tau JM_JP}$. (We take this opportunity to correct an obvious misprint in (32) of this paper. The square root operator should be applied to all the reduced masses in this equation as well as in (33).) Similar obvious replacement should be done for the corresponding terms in (33), (36) and (37). Here, $t_{i\nu}$ is an element of the unitary transformation matrix $\mathbf{T}$ between the dipole states and the states in the $(l_1 l_2)$ representation and $\mathbf{T}$ is obtained from the diagonalization of matrix $\mathbf{Q}$ with elements $Q_{ij} \equiv l_2(l_2+1)\delta_{ij} + 2\mu_2^\tau \prod_{ij}^\tau$ and

$$\Pi_{ij}^\tau \equiv \left[\sqrt{n^2-(l_1^i+1)^2}\,\delta_{l_1^j l_1^i+1} + \sqrt{n^2-l_1^{i2}}\,\delta_{l_1^j l_1^i-1}\right]\frac{3n}{2}(-1)^{J+l_2^i+l_2^j}\begin{Bmatrix} J & l_2^j & l_1^j \\ 1 & l_1^i & l_2^i \end{Bmatrix}$$
$$\times\sqrt{(2l_1^i+1)(2l_2^i+1)(2l_1^j+1)(2l_2^j+1)}$$
$$\times\begin{pmatrix} l_1^i & 1 & l_1^j \\ 0 & 0 & 0 \end{pmatrix}\begin{pmatrix} l_2^i & 1 & l_2^j \\ 0 & 0 & 0 \end{pmatrix}\begin{cases} Z_1\left[\dfrac{1}{Z_2 m_3}-\dfrac{1}{Z_3 m_2}\right] & \text{if } \tau=\beta \\ Z_2\left[\dfrac{1}{Z_3 m_1}-\dfrac{1}{Z_1 m_3}\right] & \text{if } \tau=\gamma \end{cases} \tag{9}$$

(Percival and Seaton 1957, Bethe and Salpeter 1957) with τ referring to either the β- or the γ-set. The f and g are regular and irregular solutions of

$$\frac{\mathrm{d}^2 w_\lambda}{\mathrm{d}\rho_2^{\tau 2}} + \left[k_\lambda^2 - \frac{2\mu_2^\tau Q_c^\tau}{\rho_2^\tau} - \frac{a_\lambda}{\rho_2^{\tau 2}}\right] w_\lambda = 0 \tag{10}$$

respectively. Here a_λ are eigenvalues of matrix $\mathbf{Q}$ (or, more explicitly, of matrices $\mathbf{T}$, $\mathbf{Q}$ and diagonal matrix $\mathbf{a} \equiv \mathrm{diag}[a_1, a_2, \ldots]$ satisfying $\mathbf{QT}^\dagger = \mathbf{T}^\dagger\mathbf{a}$ (Seaton 1961)) and

$$Q_c^\tau = \begin{cases} Z_1(Z_2+Z_3) & \text{if } \tau=\beta; \\ Z_2(Z_3+Z_1) & \text{if } \tau=\gamma. \end{cases} \tag{11}$$

The $\mathbf{K}$-matrix obtained this way reflects the transition amplitude to the dipole states. To obtain cross sections for states in the $(l_1 l_2)$ representation, the S-matrices in the two representations are transformed as (Seaton 1961, Gailitis and Damburg 1963)

$$\mathbf{S}^{(l_1 l_2)} = \mathrm{e}^{\mathrm{i}l_2\pi/2}\mathbf{T}^\dagger \mathrm{e}^{-\mathrm{i}\vartheta\pi/2}\mathbf{S}^{(\mathrm{dipole})}\mathrm{e}^{-\mathrm{i}\vartheta\pi/2}\mathbf{T}\,\mathrm{e}^{\mathrm{i}l_2\pi/2}. \tag{12}$$

Here $\mathbf{S}^{(l_1 l_2)}$ is the $\mathbf{S}$-matrix in the $(l_1 l_2)$ representation; $\mathbf{S}^{(\mathrm{dipole})}$ is that in the dipole representation; l_2 is a diagonal matrix with the angular momentum quantum number of the outer particle l_2 as its diagonal elements; and ϑ is a diagonal matrix with the phases from

$$f_\lambda(\rho_2) \sim \sin(k_\lambda\rho_2 - \vartheta_\lambda\pi/2) \tag{13}$$

or

$$g_i(\rho_2) \sim -\cos(k_i\rho_2 - \vartheta_i\pi/2). \tag{14}$$

From the $\mathbf{S}$-matrix, the $\mathbf{K}$-matrix is then transformed accordingly (Burke and Seaton 1971).

2.3. New angular coordinates for the solution of the two-dimensional surface functions

The two-dimensional partial differential equations (6) are solved by the higher order finite element method (FEM) (Bathe and Wilson 1976, Shertzer and Levin 1991). In order to treat the two different arrangements on an equal footing, the hypersurface equation (6) is usually expressed and solved in the α-set Jacobi coordinates. In this coordinate frame, the surface functions on the (θ, ϕ)-plane are localized near the singularities of the potential surface at large values of hyper-radius. In this paper we are interested in resonances and excitation and positronium formation cross sections to excited states, and thus the matching radius R_0 has to be chosen at a large value. The solution of (6) using even higher order FEM is unable to reach the needed accuracy. Archer *et al* (1990) introduced modified surface functions which removed the exponential factors from the lowest hydrogenic atomic state and the lowest positronium state. But even with that procedure the accuracy of their lowest energies is still only about 1%. The energies of the higher states are probably even less accurate. We have found a new transformation which allows us to solve (6) more accurately. The idea is to treat both dissociation arrangements on equal footing and at the same time that the singularity in the potential surface is changed from point-like singularity to line-like singularity. The line-like singularity in two dimensions can be easily treated using the FEM basis which is the direct product of two one-dimensional local basis functions.

The new coordinate transformation in the θ–ϕ-plane is defined as $(\theta, \phi) \rightarrow (\theta', \phi')$ with θ' as the angle between ρ_1^β and ρ_1^γ (see figure 3) and $\tan\phi' = \cos\phi^\beta / \cos\phi^\gamma$. Their ranges are $\pi \geqslant \theta' \geqslant 0$ and $\pi/2 \geqslant \phi' \geqslant 0$, respectively. To impose proper boundary conditions we also rescale the channel functions $\Phi_{\mu I}(\theta, \phi)$ to $\Phi^t_{\mu I}(\theta', \phi')$

$$\Phi_{\mu I}(\theta, \phi) \rightarrow \Phi^t_{\mu I}(\theta', \phi') = \frac{\sin\phi' \cos\phi'}{\sin\phi \cos\phi} \Phi_{\mu I}(\theta, \phi) \tag{15}$$

with $\Phi^t_{\mu I}|_{\phi'=\frac{\pi}{2}} = \Phi^t_{\mu I}|_{\phi'=0} = 0$. In the (θ', ϕ')-plane the concentration of wavefunctions in either dissociation limit are as shown in the lower frame of figure 3, i.e. they concentrate on either one of two boundaries $\phi' = 0$ and $\phi' = \pi/2$. After these transformations it can be shown that $\Phi^t_{\mu I}$ satisfies

$$\left[-\frac{C_m^2 \cos^6\phi'}{\cos^6\phi^\gamma} \frac{\partial}{\partial\phi'} \left(\frac{\cos^2\phi^\beta}{\sin^2\phi'} \frac{\partial}{\partial\phi'} \right) - \frac{C_m^2}{\cos^4\phi^\beta \cos^2\phi^\gamma \sin\theta'} \frac{\partial}{\partial\theta'} \left(\cos^2\phi^\beta \sin\theta' \frac{\partial}{\partial\theta'} \right) \right.$$
$$\left. -d(\theta', \phi') + \frac{I^2}{\sin^2\phi \cos^2\phi \sin^2\theta} + \frac{J(J+1) - 2I^2}{\cos^2\phi} + 2\mu R_a C \right]$$
$$\times \Phi^t_{\mu I}(R_a; \theta', \phi') = 2\mu R_a^2 U_{\mu I}(R_a) \Phi^t_{\mu I}(R_a; \theta', \phi') \tag{16}$$

with

$$d(\theta', \phi') \equiv \left[\frac{\partial^2 h}{\partial\phi^2} + \frac{1}{\sin^2\phi \cos^2\phi \sin\theta} \frac{\partial}{\partial\theta} (\sin\theta \frac{\partial}{\partial\theta}) h \right]$$
$$h \equiv \frac{\sin\phi \cos\phi}{\sin\phi' \cos\phi'}$$
$$C_m \equiv f_1 g_2 + f_2 g_1$$
$$f_1 \equiv \sqrt{\frac{m_2(m_1 + m_2 + m_3)}{(m_1 + m_2)(m_2 + m_3)}}$$

$$f_2 \equiv \sqrt{\frac{m_3 m_1}{(m_1+m_2)(m_2+m_3)}}$$

$$g_1 \equiv \sqrt{\frac{m_1(m_1+m_2+m_3)}{(m_1+m_2)(m_3+m_1)}}$$

$$g_2 \equiv \sqrt{\frac{m_2 m_3}{(m_1+m_2)(m_3+m_1)}}\,.$$

The normalization for $\Phi'_{\mu I}$ is

$$\int |\Phi'_{\mu I}(R_a;\theta',\phi')|^2 \left(\frac{\cos^2\phi^\beta \cos^4\phi^\gamma}{\sin^2\phi' \cos^4\phi'}\right) \sin\theta' \,\mathrm{d}\phi' \,\mathrm{d}\theta' = 1\,. \tag{17}$$

Using these two new angles, the calculated two lowest $U_{\mu 0}$ of equation (6) for $J = 0^-$ at $R_a = 160.655$ are -1.0000180 and -0.5002916, which are to be compared with the values obtained from the asymptotic expansion formula $-1.0000194 + \mathrm{O}(1/R^4)$ and $-0.5002917 + \mathrm{O}(1/R^4)$, respectively (Cavagnero *et al* 1990). If we solve (6) using the two original angles, we are unable to achieve even 1% accuracy at such a large hyper-radius with the same number of FEM bases (that is 4032 in the current calculation).

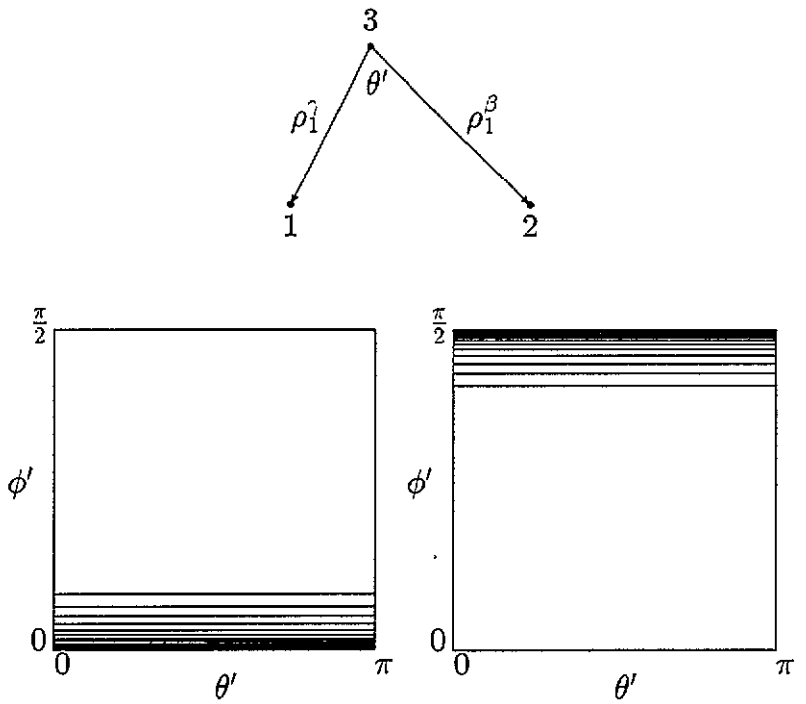

Figure 3. Upper figure: definition of θ': $\cos\theta' = \hat{\rho}_1^\beta \cdot \hat{\rho}_1^\gamma$. Lower frames: distributions (schematic) of the contour lines for channel functions in each dissociation limit on the (θ', ϕ') plane. The left-hand frame is for dissociated states described by the β-set coordinates; the right-hand frame is for states described by the γ-set coordinates.

3. Results and discussion

3.1. The S-wave resonances and cross sections

3.1.1. Energies below the H(n = 2) threshold. The results of the hyperspherical close coupling calculation in this energy region have been reported previously in Zhou and Lin (1994) using 20 hyperspherical channel functions in the inner region and the matching radius R_0 was chosen at 29.93 au. Here we have repeated the calculation using 40 channel functions and varied the matching radius to further check the accuracy and the convergence of the HSCC method.

Table 1. S-wave elastic (σ_{11}) and positronium formation into $n = 1$ (σ_{12}) cross sections at different matching radii R_0 (in atomic units) in the Ore gap. Variational results are from Brown and Humberston's calculation (1985). The cross sections are in units of πa_0^2.

	$R_0 = 29.93$		$R_0 = 250.655$		Variational	
k	σ_{11}	σ_{12}	σ_{11}	σ_{12}	σ_{11}	σ_{12}
0.71	0.0238	0.003 94	0.0306	0.003 97	0.026	0.0041
0.75	0.0415	0.004 27	0.0500	0.004 27	0.043	0.0044
0.80	0.0624	0.004 83	0.0740	0.004 83	0.065	0.0049
0.85	0.0862	0.005 57	0.0966	0.005 57	0.085	0.0058

In table 1 we list the S-wave cross sections for elastic and positronium formation into the Ps($n = 1$) state at four different energies and the dependence of the results on the matching radius R_0 and compare the results with those from the variational calculation (Brown and Humberston 1985). Two values of the matching radius were used, at $R_0 = 250.655$ and $R_0 = 29.93$, respectively.

We first look at the positronium formation cross sections. Obviously the results are very insensitive to the variation of the matching radius (to within 1%) and agree very well with the variational results of Brown and Humberston (1985). For the elastic scattering cross sections, the dependence with respect to the matching radius is more pronounced. In fact, if we take the variational results as the benchmark, we notice from table 1 that the results from the HSCC matched at $R_0 = 29.93$ appear to be better than those matched at $R_0 = 250.655$. This is not entirely surprising and is the consequence of using the diabatic-by-sector method in our approach. In the diabatic-by-sector method, the potential curve does not approach the asymptotic limit correctly. It has been shown (Macek 1968) that the asymptotic potential curves approach the correct limit only if the diagonal non-adiabatical coupling term $W_{\nu\nu} \equiv \langle \Phi_\nu | \, \mathrm{d}^2/\mathrm{d}R^2 | \Phi_\nu \rangle$ is included as a part of the adiabatic potential. This is the case in the standard adiabatic approach, but not in the diabatic-by-sector method. Since the $W_{\nu\nu}$ term behaves like $1/R^2$ asymptotically, this effect can be accounted for in the diabatic-by-sector method by coupling the increasing number of hyperspherical channel functions when R is increased. In the present calculation, we have fixed the number of channels in the inner region to 40 even at the large matching radius $R_0 = 250.655$. This results in an inaccurate account of the $W_{\nu\nu}$ term at large R. Since this $W_{\nu\nu}$ term is always positive, the error is that the effective potential for the elastic scattering channel is too attractive and thus the calculated cross sections are too large. In table 1, we do note that the elastic scattering cross sections calculated using the larger matching radius are too large. To achieve better convergence when such a large matching radius is used, one would have to increase the number of hyperspherical channel functions in the inside region. We note

that the above remark has less effect on the positronium formation cross section since the transition is dominated by the off-diagonal coupling term.

We also remark that the elastic scattering cross sections using the HSCC method but different numerical approaches do give somewhat different results. Igarashi and Toshima (1994) obtained results which are about 15% worse than ours. They chose a matching radius at about 400–500 au but only nine channels in the inner region. Archer *et al* (1990) included 43 channels in the inner region, but the accuracy of their potential curves and coupling terms are more limited. To achieve high precision in the HSCC method, numerical accuracy within the prescribed approximation is very important.

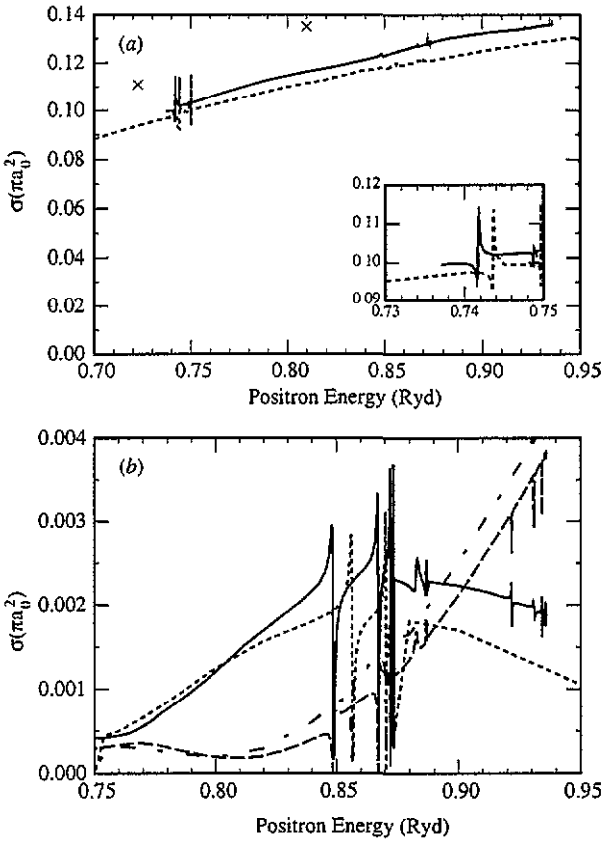

Figure 4. (*a*) Elastic scattering cross sections for the S-wave: full curve, present calculation; dotted curves, from CC(6, 6) of Mitroy and Ratnavelu (1995); crosses, from Igarashi and Toshima (1994). (*b*) The S-wave excitation cross sections into H(2s) and H(2p) states. For the 2s state: full curves, present calculation; dotted curves, Mitroy and Ratnavelu (1995). For the 2p state: broken curves, present result; chain curves, Mitroy and Ratnavelu (1995).

3.1.2. S-wave elastic and H($n = 2$) excitation cross sections. We next examine the S-wave partial cross sections for energies near and above the H($n = 2$) threshold. To begin with, we mention that the inelastic threshold for H($n = 2$) is at 0.75 Ryd, for Ps($n = 2$) is at 0.875 Ryd, for H($n = 3$) is at 0.8889 Ryd, for H($n = 4$) is at 0.9375 Ryd and for Ps($n = 3$)

is at 0.9444 Ryd. In figure 4(*a*) the elastic scattering cross sections for energy in the 0.70–0.95 Ryd region from the present calculation are shown together with the close coupling results of Mitroy and Ratnavelu (1995) which included six atomic states on the H-atom centre and six states of the positronium. Such a calculation is abbreviated as CC(6, 6). Their results are shown as dotted curves. The overall agreement is reasonable in terms of the absolute values and the energy dependence. Also shown in the figure are the results from Igarashi and Toshima (1994) at two energy points. The HSCC calculations by Archer *et al* (1990) are in good agreement with ours, except that their results show some small ripples over a wide energy.

In figure 4(*a*) we note that there are resonances in the elastic scattering cross sections at energies below the H($n = 2$) threshold. Further analysis of these resonances is given in section 3.1.4. We only point out that the resonance positions as shown in figure 4(*a*) indicate clearly that our predictions are different from those of the CC(6, 6) calculations. Figure 4(*a*) also shows some tiny resonance structures at energies above the H($n = 2$) threshold. These resonances occur at energies below the Ps($n = 2$), H($n = 3$), etc, thresholds. They are more clearly seen by examining the inelastic scattering cross sections to H(2s) and H(2p) states, as shown in figure 4(*b*) where the H(2s) excitation cross sections from the HSCC are shown as full curves, and those from CC(6, 6) are shown as dotted curves. The energy dependences in the two calculations are similar, but again the resonance energies (lying below the Ps($n = 2$) threshold) obtained using CC(6, 6) do not agree with those from the HSCC calculation.

In figure 4(*b*) we also display the H(2p) excitation cross sections (broken curves) and compare with the result from CC(6, 6), (chain curves). We note that the relative magnitude and the energy dependence in the two calculations are quite similar, but the resonance parameters obtained in CC(6, 6) appear to be inaccurate. We also note that additional resonances occur at higher energies as the new inelastic thresholds are open.

3.1.3. S-wave Ps formation cross sections to 1s, 2s and 2p states. The positronium formation cross section to Ps(1s) is shown in figure 5(*a*) over the 0.70–0.95 Ryd region. Also shown are those from the CC(6, 6) calculation by Mitroy and Ratnavelu (1995). The agreement between the two calculations is quite good except for the resonance positions. The results from Igarashi and Toshima (1994) at two energy points, shown as crosses, also agree with ours well.

We have also calculated the partial cross sections for positronium formation to 2s and 2p states. The results are shown in figure 5(*b*). These cross sections are about one order of magnitude smaller than to the Ps(1s) state and show little energy dependence in the energy range considered. We also check (not shown) our results with the calculations of Archer *et al* (1990). Although the magnitudes in the two calculations are quite close, the shape is not the same. They observed a valley near $E \simeq 0.878$ Ryd which does not correspond to any resonance. Second, our cross section above the H($n = 3$) threshold is smooth with respect to the increase of collision energy whereas theirs is not. We suspect that the discrepancy is due to the limited numerical accuracy in their calculation, and possibly also because they did not match the asymptotic solutions to dipole states.

3.1.4. The S-wave resonances. From figures 4 and 5, it is evident that there are numerous resonances near each inelastic threshold. In the HSCC method, these resonances can be 'traced' by solving the hyper-radial equation over a fine set of mesh points over the typical width of each resonance. This causes no numerical difficulty since the solution of coupled differential equations is not time consuming. From the calculated total phase shift (the

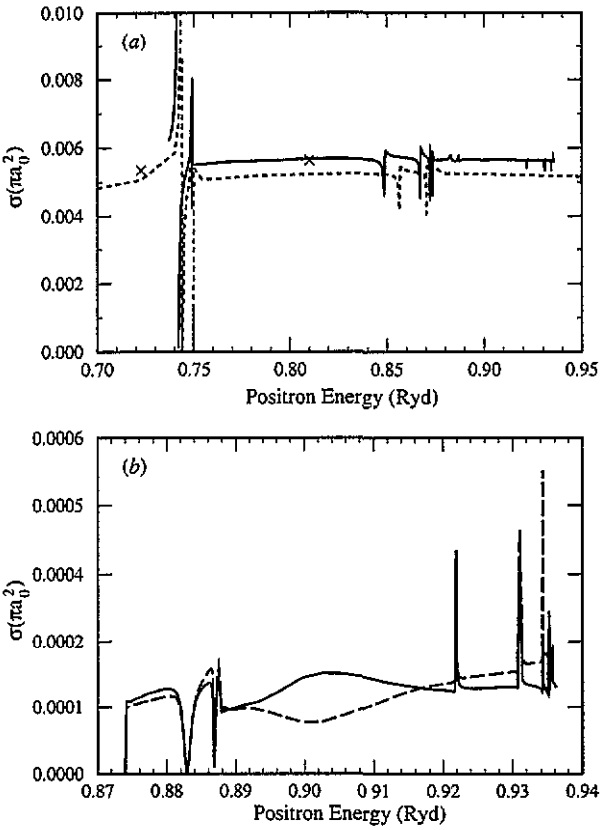

Figure 5. The S-wave positronium formation cross sections into (*a*) Ps($n = 1$) and (*b*) Ps($n = 2$) states with respect to the incident energy of the positron. In (*a*): full curve, present result; dotted curve, Mitroy and Ratnavelu (1995); crosses, Igarashi and Toshima (1994). In (*b*): full curve, present Ps(2s) formation cross sections; broken curves, present Ps(2p) cross sections. Note the resonances associated with the Ps($n = 2$) threshold at 0.875 Ryd, and the H($n = 3$) threshold at 0.8889 Ryd and the H($n = 4$) threshold at 0.9375 Ryd.

sum of the eigenphases), the resonance position and its total width are obtained by fitting the total phase shift to $\delta = \text{constant} - \arctan\left(\frac{1}{2}\Gamma/(E_R - E)\right)$. The resulting resonance parameters are listed in table 2. These parameters have also been calculated variationally for each individual states using the complex-coordinate rotation method and the results are also shown in table 2 for comparison.

We list only a few resonances below each threshold. Because of the asymptotic dipole potential there is a whole series of resonances below each threshold, and for the higher members the energy levels should follow the relation $\epsilon_{n+1}/\epsilon_n = \mathrm{e}^{-2\pi/\zeta}$ (Greene 1980) where $\zeta = \sqrt{a_\lambda - 0.25}$, with a_λ being the permanent dipole moment as seen in (10) and that energy ϵ is measured from the threshold. The higher resonances are very close to the threshold and very narrow and are not examined.

Below the H($n = 2$) threshold, only two resonances are calculated, the positions and widths are in good agreement with those from complex-coordinate rotation calculations. In the HSCC approach, one can identify these resonances approximately as bound states associated with individual adiabatic potential curves. For example, in figure 6 we show the lowest adiabatic potential curves that converge to the H($n = 2$) threshold and to the

Table 2. Positions and widths of S-wave resonances. Results of complex-coordinate rotation calculations are from Ho (1992).

Present		Complex rotation	
E (Ryd)	$\frac{1}{2}\Gamma$ (Ryd)	E (Ryd)	$\frac{1}{2}\Gamma$ (Ryd)
	Below H($n = 2$) threshold		
−0.257 312	6.64(−5)	−0.257 2453	6.66(−5)
−0.250 302	3.91(−6)	−0.250 17	< 1.0(−5)
	Below Ps($n = 2$) threshold		
−0.150 316	3.342(−4)	−0.150 279	3.35(−4)
−0.131 704	1.624(−4)	−0.131 659	1.63(−4)
−0.126 806	5.03(−5)	−0.126 774	4.8(−5)
−0.125 47	1.58(−5)		
	Below H($n = 3$) threshold		
−0.116 101	6.161(−4)	−0.116 06	6.2(−4)
−0.112 100	1.300(−4)	−0.112 06	1.4(−4)
	Below H($n = 4$) threshold		
−0.077 100	4.762(−5)	−0.077 063	4.76(−5)
−0.067 902	4.782(−5)	−0.067 876	4.8(−5)
−0.064 625	1.625(−5)	−0.064 682	2.2(−5)
−0.063 725	4.884(−5)	−0.063 699	5.0(−5)
−0.063 304	2.7(−6)	−0.063 259	1.0(−5)

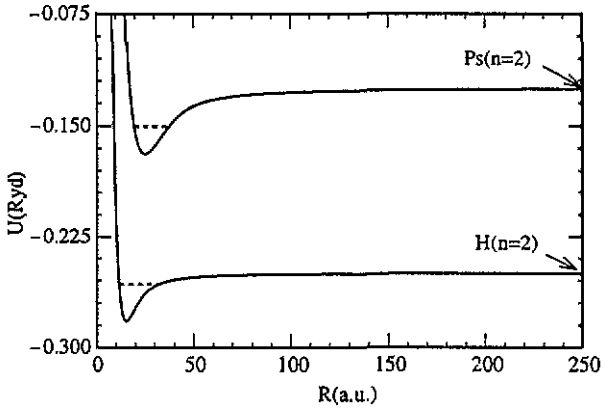

Figure 6. The S-wave adiabatic hyperspherical potential curves that converge to the H($n = 2$) and Ps($n = 2$) thresholds. Two other curves converging to each limit are not shown here since they are repulsive and support no resonances. The lowest resonant state in each potential is indicated by a horizontal dotted line.

Ps($n = 2$) threshold. The position of the lowest resonance below each threshold is indicated by a horizontal dotted line in the figure. We mention that the resonance positions calculated using CC(6, 6) are not in agreement with the results shown in table 2, as illustrated in the inset in figure 4(*a*).

Below the Ps($n = 2$) threshold, four resonances are identified in the current calculation. The first three agree well with the variational results. We also indicate that the lowest resonance is associated with the lowest potential curve below the Ps($n = 2$) threshold, as illustrated in figure 6. A resonance at $E = -0.222$ Ryd was previously reported by Doolen (1978). We did not find such a resonance, and from the potential curves shown in figure 6,

no such resonance is expected. The resonances predicted from the CC(6, 6) calculations in this energy region also do not agree with the results shown in table 2.

Below the H($n = 3$) threshold two resonances were calculated. The position and width of each state obtained by HSCC are in good agreement with those from the variational calculation (Ho 1992). The lowest resonance is a bound state associated with the lowest adiabatic potential curve below the H($n = 3$) threshold, as shown in figure 7. This potential curve crosses with the repulsive curve that converges to the Ps($n = 2$) threshold. This crossing is treated as diabatic in the present model.

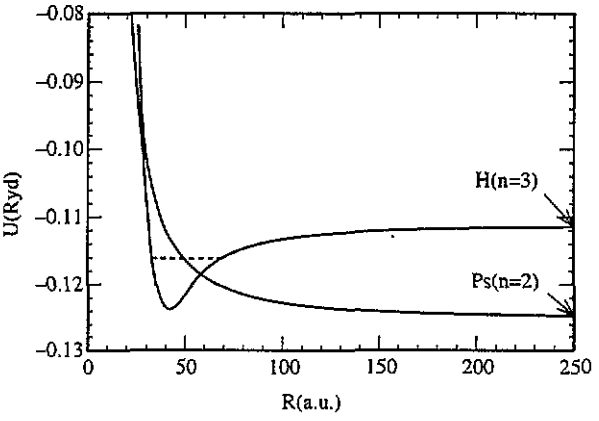

Figure 7. The S-wave adiabatical hyperspherical potential curves that converge to the Ps($n = 2$) and H($n = 3$) thresholds. The attractive curve converging to Ps($n = 2$) is not shown since it does not cross the H($n = 3$) curve. The lowest resonant state associated with the attractive potential is indicated by a horizontal dotted line.

Below the H($n = 4$) threshold five resonances have been calculated and all agree well with the variational results except for the highest one. Because the energy gap between Ps($n = 3$) and H($n = 4$) is only about 0.0069 Ryd, the resonance series below H($n = 4$) and Ps($n = 3$) actually overlap with each other. These overlapping resonances have been studied in our previous paper (Zhou and Lin 1995a).

3.2. The P-wave cross sections

3.2.1. Partial scattering cross sections. The P-wave elastic and positronium formation into the ($n = 1$)-level cross sections are shown in figure 8(*a*). We include 34 channels in this calculation, 25 for $I = 0$ and nine for $I = 1$. Two-dimensional matching is carried out at $R_0 = 250.655$. For the elastic scattering cross sections, our results are about 10% less than the results from the CC(6, 6) calculation of Mitroy and Ratnavelu (1995). We believe that the CC(6, 6) results are more accurate. To achieve higher precision in the present approach, more channels should be included. In figure 8(*a*), the elastic scattering cross sections calculated by Igarashi and Toshima (1994) are also shown. Their results are slightly less than ours.

In figure 8(*a*) we also show the P-wave positronium formation into the ($n = 1$)-level cross section. Our results agree with the CC(6, 6) calculations to within 1% except near the resonance region. As shown in the inset window, the resonances predicted in the CC(6, 6) calculation are believed to be inaccurate, as in the S-wave cases. The results from Igarashi and Toshima (1994) at the two energy points shown are also in agreement with our results.

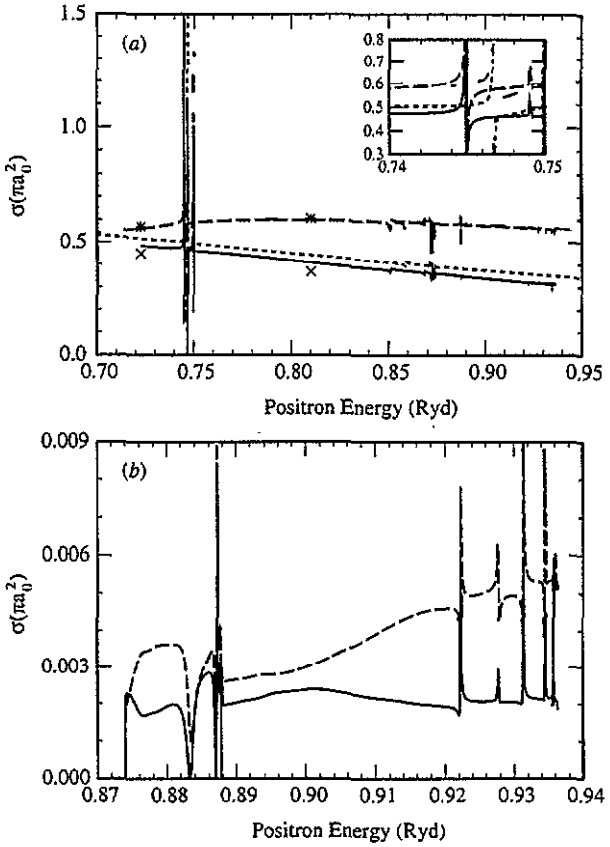

Figure 8. (*a*) Cross sections for the P-wave elastic and positronium formation into the Ps($n = 1$) state. For the elastic scattering cross sections: full curves, present calculation; dotted curve, from CC(6, 6) of Mitroy and Ratnavelu (1995); crosses, from Igarashi and Toshima (1994). For the positronium formation to Ps($n = 1$): broken curves, present result; chain curves, from CC(6, 6) of Mitroy and Ratnavelu (1995). Note that the two sets of curves overlap and are indistinguishable except in the resonance region, see the inset window. The asterisks are from Igarashi and Toshima (1994). (*b*) The P-wave positronium formation cross sections to Ps(2s) (full curves) and to Ps(2p) (broken curves) from the HSCC calculation.

In figure 8(*b*), we show the P-wave positronium formation cross sections to Ps(2s) and Ps(2p) states. These cross sections are quite small, about two orders of magnitude less than the cross sections for positronium formation to the Ps($n = 1$) state. There are no other extensive calculations available for comparison.

The P-wave excitation cross sections to H(2s) and H(2p) states are shown in figure 9(*a*). The results are in good agreement with those from the CC(6, 6) calculations except in the resonance energy region. Similarly, in figure 9(*b*) we show the excitation cross sections to H(3s, 3p, 3d) states.

3.2.2. The P-wave resonances. Figures 8 and 9 show that the inelastic scattering cross sections are dominated by pronounced resonances. We have analysed a number of resonances and their positions and widths are listed in table 3 and are compared with those from the variational calculations using the complex-coordinate rotation method (Ho 1990). When comparison is possible, we found good agreement between the two calculations, but

Table 3. Positions and widths of P-wave resonances. Results of complex-coordinate rotation calculations are from Ho (1990).

Present		Complex rotation	
E (Ryd)	$\frac{1}{2}\Gamma$ (Ryd)	E (Ryd)	$\frac{1}{2}\Gamma$ (Ryd)
	Below H($n = 2$) threshold		
−0.254 132	8.152(−6)	−0.254 112	8.1(−6)
−0.250 11	2.1(−7)		
	Below Ps($n = 2$) threshold		
−0.148 071	2.936(−4)	−0.148 181	2.97(−4)
−0.130 666	1.480(−4)	−0.130 73	1.67(−4)
−0.127 343	6.73(−5)	−0.127 33	7.3(−5)
−0.126 347	2.39(−5)		
−0.125 307	1.04(−5)		
	Below H($n = 3$) threshold		
−0.115 626	5.71(−4)		
−0.111 953	1.167(−4)		
−0.111 70	6.61(−6)		
−0.111 169	3.74(−5)		
	Below H($n = 4$) threshold		
−0.076 673	5.289(−5)		
−0.071 211	5.698(−5)		
−0.067 585	4.666(−5)		
−0.064 520	1.31(−5)		
−0.064 360	2.81(−5)		

we have extracted many more resonances. Below the H($n = 2$) threshold, two resonances from CC(6, 6) calculations have been identified, but they are again at higher energies as shown in the inset window of figure 8(*a*).

The lowest resonance below the H($n = 2$) threshold is associated with the lowest potential curve that converges to the H($n = 2$) threshold, as indicated in figure 10. To reveal the relation between the S- and P-wave resonances, we check the validity of whether the latter can be approximated by adding one unit of rotational excitation to the former. In other words, can the P-wave potential curve be obtained by adding $J(J+1)/R^2 (= 2/R^2)$ to the S-wave potential curve? This was carried out and the resulting potential curve is shown in figure 10 by the broken curves. We note that it is in very good agreement with the P-wave potential curve actually calculated. This demonstrates that the rotor structure discussed by Chen and Lin (1990) is valid for the present system in this energy region.

Below the Ps($n = 2$) threshold five resonances have been calculated. It is found that the third resonance does not asymptotically follow the scaling relation $\epsilon_{n+1}/\epsilon_n = \exp(-2\pi/\zeta)$ expected from a potential with attractive dipole behaviour. Using the known dipole moment for the lowest potential curve below the Ps($n = 2$), $\epsilon_{n+1}/\epsilon_n = 0.256$ is expected. From the actual calculated resonances, $\epsilon_2/\epsilon_1 = 0.2456$ and $\epsilon_3/\epsilon_2 = 0.4136$. Thus the third resonance does not follow the scaling relation. In fact, $\epsilon_4/\epsilon_2 = 0.2381$ is closer to the expected ratio. We thus easily identify that the third resonance belongs to a different group. In figure 11 we show the two lowest potential curves that converge to the Ps($n = 2$) threshold. The upper curve supports the third resonance while the other resonances all belong to the lower curve. We note that the upper curve, which has an attractive potential well at small R, is repulsive at large R. Such a potential can typically support shape resonances. In the present case, the attractive well is strong enough such that a resonance lies below the asymptotic threshold. Energetically it is like a typical Feshbach resonance.

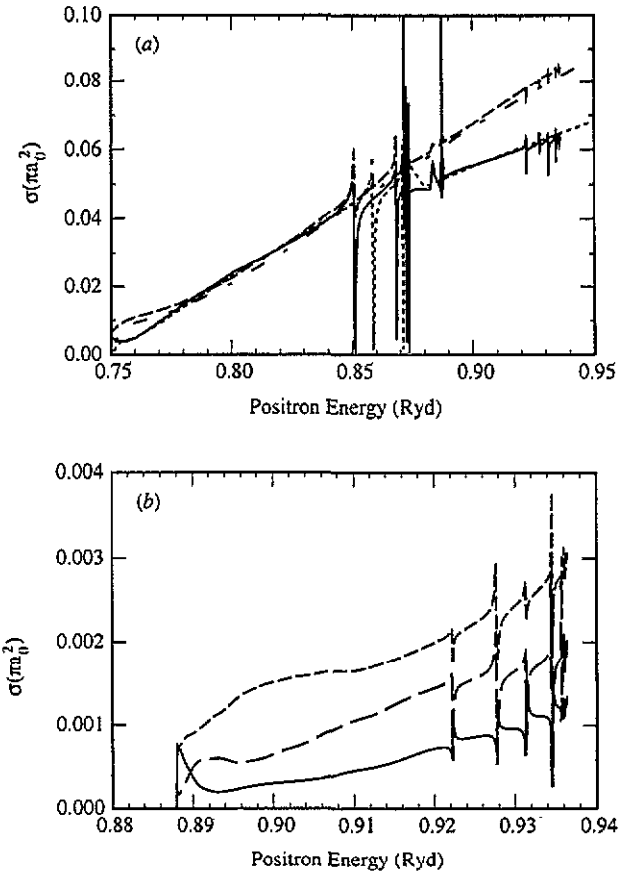

Figure 9. (*a*) The P-wave excitation cross sections into H(2s) and H(2p) states. For the 2s state: full curves, present calculation; dotted curves, Mitroy and Ratnavelu (1995). For the 2p state: broken curves, present result; chain curves, Mitroy and Ratnavelu (1995). (*b*) Excitation cross sections to H(3s) (full curves), H(3p) (broken curves) and H(3d) (long-broken curves) states from the present calculation.

The resonances at higher energies become increasingly difficult to analyse. In figure 12(*a*) we show two of the five adiabatic potential curves that converge to the H($n = 3$) threshold. These two curves can support 'bound' states, but they cross the uppermost curve that converges to the Ps($n = 2$) threshold. The lowest curve that converges to the H($n = 3$) threshold has been found to follow the rotational structure very well. A very careful examination will show that there are actually two curves overlapping almost completely. The curve obtained by adding $2/R^2$ to the corresponding S-wave curve is found to differ little from the curve actually calculated.

The spectra become increasingly more complex at even higher energies. In figure 12(*b*) we show the adiabatic potential curves that converge to the H($n = 4$), Ps($n = 3$) and some that converge to H($n = 5$) thresholds. There are numerous crossings which would make the analysis of each resonance rather tedious. On the other hand, the HSCC method, which uses diabatic basis states, can be used to perform calculations even if a much larger number of channels are included. These higher resonances are not analysed here.

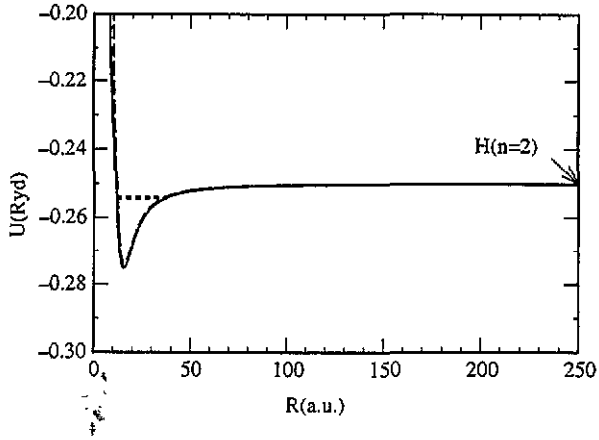

Figure 10. P-wave potential curves converging to H($n = 2$): full curve, the calculated attractive P-wave adiabatic potential curve; broken curve, obtained by adding $2/R^2$ to the attractive S-wave adiabatic potential converging to H($n = 2$). The other two potential curves converging to this limit are repulsive and are not shown. The lowest P-wave resonant state in the attractive potential is indicated by a horizontal dotted line.

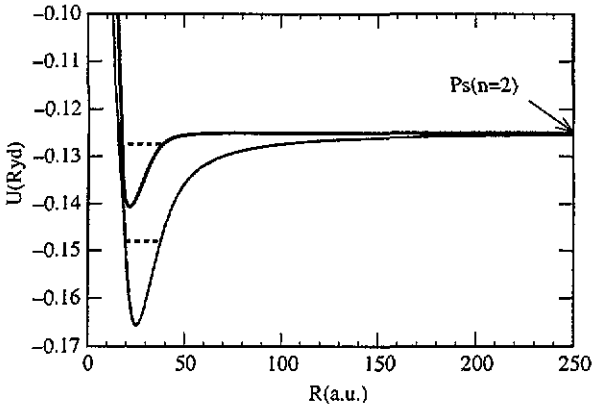

Figure 11. P-wave potential curves converging to the Ps($n = 2$) limit: full curves, the calculated P-wave attractive adiabatic potential curves; broken curve (on top of the lowest curve and barely visible), obtained by adding $2/R^2$ to the attractive S-wave adiabatic potential converging to Ps($n = 2$). The lowest resonant state in each attractive P-wave potential is indicated by a horizontal dotted line.

4. Conclusion

We show in this paper that the hyperspherical close coupling method can be used to calculate positron–hydrogen atom scatterings up to the higher energy region where many channels are open. By use of a new two-dimensional coordinate transformation the hyperspherical potentials at large hyper-radii can be calculated accurately. Despite the lack of experimental data to check the results of this calculation, we are confident that the results are reliable since the positions and widths of resonances below each inelastic threshold obtained using the HSCC method are as accurate as those obtained variationally using the complex-coordinate rotation method. For the inelastic scattering cross sections, we have shown that our results

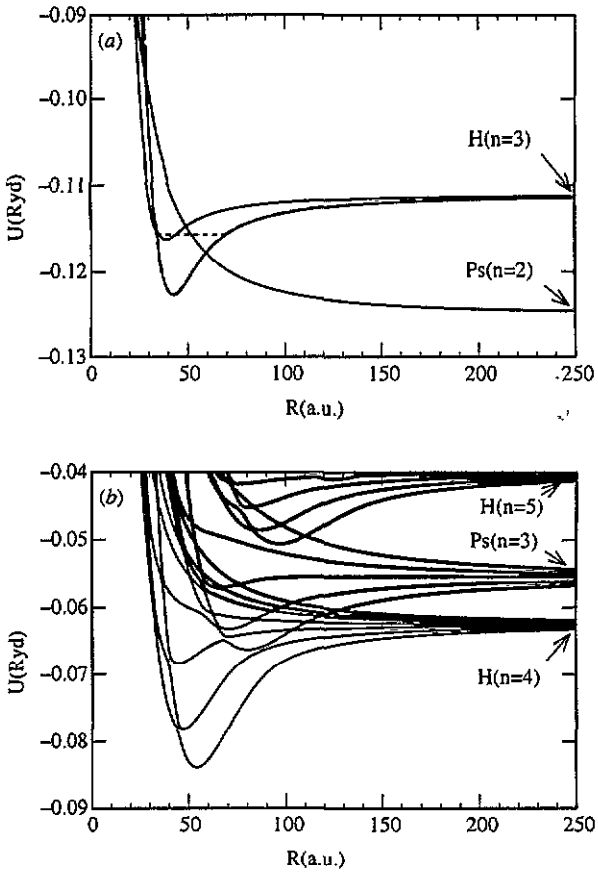

Figure 12. (*a*) The P-wave adiabatical potential curves converging to Ps($n = 2$) and H($n = 3$) thresholds: full curves, the calculated P-wave adiabatic potential curves; broken curves, obtained by adding $2/R^2$ to the S-wave adiabatic potential. There are two additional attractive curves converging to Ps($n = 2$) that are not shown in this figure. The lowest P-wave resonant state in the attractive potential is indicated by a horizontal dotted line. (*b*) The high-lying P-wave adiabatic potential curves.

are in agreement with the more extensive close coupling calculations. These results, together with the relative stability of the calculations with respect to the number of basis functions used and the matching radius varied, make us believe that the results presented here are accurate. We have illustrated the power of HSCC for treating rearrangement collisions, even in energy regions where many channels are open. This conclusion is particularly relevant to applications of the HSCC method to other three-body systems such as in atom–diatom reactive scattering where the interaction potential surface is less well known. Once the numerical accuracy is achieved in the HSCC calculations, the discrepancy between experiment and calculations probably should be attributed to other sources of errors, such as the quality of the potential surface, or the reliability of experimental data.

Acknowledgments

This work was supported in part by the US Department of Energy, Office of Energy

Research, Office of Basic Energy Sciences, Division of Chemical Sciences. The calculations using the FEM were conducted using the resources of the Cornell Theory Center, which receives major funding from the National Science Foundation and IBM Corporation, with additional support from the New York State Science and Technology Foundation and members of the Corporate Research Institute. We are also grateful to Dr Yudong Wang for helpful discussions.

References

Archer B J, Parker G A and Pack R T 1990 *Phys. Rev.* A **41** 1303
Basu M, Mukherjee M and Ghosh A S 1989 *J. Phys. B: At. Mol. Opt. Phys.* **22** 2195
Bathe K and Wilson E 1976 *Numerical Methods of Finite Element Analysis* (Englewood Cliffs, NJ: Prentice-Hall)
Bethe H A and Salpeter E E 1957 *Quantum Mechanics of One- and Two-Electron Atoms*
Bhatia A K and Temkin A 1964 *Rev. Mod. Phys.* **36** 1050
Brown C J and Humberston J W 1985 *J. Phys. B: At. Mol. Phys.* **18** L401–6
Burke P G and Seaton M J 1971 *Method. Comput. Phys.* **10**
Cavagnero M, Zhen Z and Macek J 1990 *Phys. Rev.* A **41** 1225
Chen Z and Lin C D 1990 *Phys. Rev.* A **42** 18
Doolen G D, Nuttal J and Wherry C 1978 *Phys. Rev. Lett.* **40** 313
Gailitis M and Damburg R 1963 *Proc. Phys. Soc.* **82** 192
Greene C H 1980 *Phys. Rev.* A **22** 149
Higgins K and Burke P G 1991 *J. Phys. B: At. Mol. Opt. Phys.* **24** L343
Ho Y K 1990 *J. Phys. B: At. Mol. Opt. Phys.* **23** L419
—— 1992 *Hyperfine Interactions* **73** 109
Humberston J W and Armour E A G 1987 *Atomic Physics With Positrons* (New York: Plenum)
Igarashi A and Toshima N 1994 *Phys. Rev.* A **50** 232
Kernohan A A, McAlinden M T and Walters H R 1994 *J. Phys. B: At. Mol. Opt. Phys.* **27** L625
Launay J M 1993 *Dynamical Processes in Molecular Physics* ed G Delgado Barrio (Bristol: IOP Publishing) pp 97–120
Lin C D 1984 *Phys. Rev.* A **29** 1019
—— 1986 *Adv. At. Mol. Phys.* **22** 77
—— 1995 *Phys. Rep.* **257** 1
Macek J H 1968 *J. Phys. B: At. Mol. Phys.* **1** 831
Mitroy J and Ratnavelu K 1995 *J. Phys. B: At. Mol. Opt. Phys.* **28** 287
Percival I C and Seaton M J 1957 *Proc. Camb. Phil. Soc.* **53** 654
Sarkar N K, Basu M and Ghosh A S 1993 *J. Phys. B: At. Mol. Opt. Phys.* **26** L79
Seaton M J 1961 *Proc. Phys. Soc.* **77** 174
Shertzer J and Levin F S 1991 *Phys. Rev.* A **43** 2531
Smith F T 1960 *Phys. Rev.* **120** 1058
Tang J Z and Shimamura I 1995 *Phys. Rev.* A **51** R1738
Tang J Z, Watanabe S and Matsuzawa M 1992 *Phys. Rev.* A **46** 2437
Zhou B, Lin C D, Tang J Z, Watanabe S and Matsuzawa M 1993 *J. Phys. B: At. Mol. Opt. Phys.* **26** 2555
Zhou Y and Lin C D 1994 *J. Phys. B: At. Mol. Opt. Phys.* **27** 5065
—— 1995a *Phys. Rev. Lett.* accepted
—— 1995b *J. Phys. B: At. Mol. Opt. Phys.* accepted